Carlos Alvarado Chavarin, Elena Hardt, Oliver Skibitzki, Thomas Voss, Mohammed Eissa, Davide Spirito, Giovanni Capellini, Leonetta Baldassarre, Julia Flesch, Jacob Piehler, Changjiang You, Sönke Grüssing, Friedhard Römer and Bernd Witzigmann*

Terahertz subwavelength sensing with bio-functionalized germanium fano-resonators

https://doi.org/10.1515/freq-2022-0078
Received April 12, 2022; accepted August 1, 2022;
published online August 15, 2022

Abstract: Localized Surface Plasmon Resonances (LSPR) based on highly doped semiconductors microstructures, such as antennas, can be engineered to exhibit resonant features at THz frequencies. In this work, we demonstrate plasmonic antennas with increased quality factor LSPRs from Fano coupling to dark modes. We also discuss the advances in the biofunctionalization of n-doped Ge antennas for specific protein immobilization and cell interfacing. Finally, albumin biolayers with a thickness of a few hundred nanometers are used to demonstrate the performance of the fano-coupled n-Ge antennas as sensors. A resonant change of over 10% in transmission, due to the presence of the biolayer, can be detected within a bandwidth of only 20 GHz.

Keywords: biosensing; fano resonances; semiconductor plasmonics; terahertz sensor.

1 Introduction

Spectroscopy and imaging in the THz frequency range can provide information with large relevance in technological, medical and security applications [1]. In the same way, "fingerprint" absorption lines of distinct gases in the IR can be used for the early detection of human diseases [2, 3] or in specialized industrial processes [4]. In particular, spectroscopy techniques in the THz range (0.3–3 THz) could enable the study of conformational modes down to the biomolecular level [5]. The lack of a "toolbox" of compact and economically viable THz devices, such as powerful sources and sensitive detectors, have impeded advances in this field. All-electronic, CMOS-based Transmission – Receiver systems (TRx) have increased their operation frequencies up to the THz range [6, 7]. Such TRx systems are highly integrated circuits that will enable compact and economic devices for THz detection [8]. However, low concentrations, low Tx power and/or the limited interaction of the THz radiation due to the relatively large wavelengths (100–1000 μm) compared to the typical analyte size in the sub-micrometer range have to be compensated to use this part of the electromagnetic (EM) spectrum for the detection of biomolecules.

To address this issue, localized surface plasmon resonances (LSPR) enable the tailoring of light-matter interactions into subwavelength volumes at virtually any desired frequency of the EM spectrum [9]. Metallic or highly doped semiconductor subwavelength structures, such as antennas, can be used to directly interact with traveling EM waves and achieve strongly localized LSPR. The EM confinement produces an enhancement of the electric field in the vicinity of the subwavelength plasmonic structures increasing the interaction of THz radiation with analytes [9]. This implies that the amount of analyte required to obtain a detectable signal could be drastically reduced, while simultaneously decreasing the overall device size. Due to their higher skin depth, caused by lower conductivity, semiconductor-based LSPR has the advantage over their metallic counterparts of a larger field penetration into the material [10]. Since LSPR are responsive to changes in their immediate surroundings, they can be used as a sensing platform. In addition (bio-) functionalization of the LSPR structures can enable selectivity of the sensor to discriminate the detection of a specific analyte [11, 12].

***Corresponding author: Bernd Witzigmann**, Department of Electrical-Electronic-Communication Engineering, Friedrich-Alexander Universität Erlangen-Nürnberg, Erlangen-Nürnberg, Germany, E-mail: bernd.witzigmann@fau.de. https://orcid.org/0000-0001-9705-9516
Carlos Alvarado Chavarin, Elena Hardt, Oliver Skibitzki, Thomas Voss, Mohammed Eissa, Davide Spirito and Giovanni Capellini, IHP GmbH, Frankfurt Oder, Germany
Leonetta Baldassarre, Department of Physics, Sapienza University of Rome, Rome, Italy
Julia Flesch, Jacob Piehler and Changjiang You, Department of Biology/Chemistry, and Center for Cellular Nanoanalytics (CellNanOs), University of Osnabrück, Osnabrück, Germany. https://orcid.org/0000-0002-7839-6397 (C. You)
Sönke Grüssing, Electrical Engineering/Computer Science Dept. and CINSaT, University of Kassel, Kassel, Germany
Friedhard Römer, Department of Electrical-Electronic-Communication Engineering, Friedrich-Alexander Universität Erlangen-Nürnberg, Erlangen-Nürnberg, Germany

In previous studies, we have presented the sensing capability of semiconductor-based LSPR devices [10, 13, 14]. In particular, we have demonstrated sensing by using highly n-doped Ge bow-tie antennas (n-Ge antenna), epitaxially grown on Si, operating in the THz range [14]. The process for obtaining the high doping in the Ge epilayers, necessary to realize quasi metallic transport conditions in the antenna, was optimized to a quality close to that of bulk Ge [14]. Consequently, a further improvement of the resonant antenna performances, i.e. an improvement of the quality (Q-) factor of the resonator, should be explored beyond the intrinsic material properties, rather pointing to new design concepts. Fano resonances are produced due to the destructive interference from two resonant modes [15]. First observed by U. Fano in He-electron scattering experiments [16], the typical asymmetric line shape in the spectrum arises when the continuous state of a resonator couple to a discrete state of another resonator. Fano-like resonances have been studied in THz metamaterials to attain sharper spectral features by the interaction between symmetric [17] and asymmetric [18, 19] composite metaunits. This interaction produces a transmission peak, analog to the Electromagnetic Induced Transparency (EIT) [20]. An important condition for the Fano resonance is that while one of the resonators is being driven directly (bright mode), the second oscillator can only increase its energy by means of coupling to the first resonator (dark mode).

In this work, we report the wafer-scale fabrication of a THz sensing platform improved through Fano coupling of a dark mode to the LSPR in n-doped Ge antenna structures. The Fano coupling occurs between the antenna resonance and continuum states of waves traveling in the substrate which appear as the latter is thinned-down. To the best of our knowledge, the application of bright-dark modes Fano resonances has not been explored in a semiconductor-based LSPR platform. Moreover, it is shown that the plasmonic n-Ge antennas platform can be biofunctionalized for site-specific protein capturing and for its selective interfacing with cells. Finally, it is demonstrated that the Fano coupling can be engineered to the desired antenna geometry and by using a high-resistivity substrate, the sharpness of its spectral features can be even further enhanced. The bright-dark coupling produces a noticeable transmission change due to the presence of a model protein layer, within bandwidths as narrow as 20 GHz.

2 Resonator design and technology

2.1 Simulations model and fabrication

The spectral response of the n-Ge antennas in the THz range can be reliably simulated by solving Maxwell's equations using a Finite Element Method (FEM), with input data such as geometry, density, arrangement and stack materials [10, 13]. Comprehensive FEM simulations have been made, using the method and parameters as described in [10]. The designed (theoretical) resonance frequency (f_0) of the plasmonic antennas is mainly governed by their arm length. Figure 1 shows an SEM image with the geometry of a single antenna. The simulation model under investigation here consists of an array of highly n-doped (10^{19} cm^{-3}) Ge bowtie antennas placed on a lightly p-doped (10^{15} cm^{-3}) Si substrate, this is regarded as the n-Ge antenna/Si (slab) substrate system. The simulation is performed only on a quarter of the antenna structure, and in the x-direction, the simulation domain is terminated by a Dirichlet boundary condition (BC), whereas for the y-direction we used the Neumann boundary condition This setup conforms with an x -polarized plane wave and ensures appropriate mirroring of the incident and scattered fields on the domain boundaries while reducing computational complexity. In the z-direction, the simulation domain is terminated with a perfectly matched layer (PML). Due to the direct excitation of the plasmonic antennas with the THz radiation their resonance is regarded as a bright mode. A second oscillator arises in the antenna/substrate system by thinning the Si wafer from the backside to a defined thickness. The substrate with a thickness of several wavelengths exhibits two types of resonances: for illumination with a TEM wave from top, Fabry-Perot resonances occur.

For in-plane excitation (parallel to the wafer surface), propagating slab waveguide modes exist. The slab mode resonance from this second oscillator presents the dark mode, since is not excited directly by the TEM THz radiation but indirectly by its interaction with the bright mode. An incident plane wave perpendicular to the Ge/Si surface polarized in the x-direction, parallel to the antenna arms (active state, $T_{\parallel}$), excites the LSPR, which leads to a decrease in the transmission spectrum (bright mode). The exited LSPR in turn can excite a guided mode in the Si slab (dark mode) that propagate in directions parallel to the substrate-air interface. The guided wave traveling can be seen in the electric field intensity simulations in Figure 1B.

Without Ge antennas, a plane wave excitation perpendicular to the Si slab excites Fabry-Perot (FP) resonances, seen as oscillations in the spectra. FP modes are standing waves due to interference of the incident light being reflected between the top and bottom interfaces. The spectral plot of the transmission in Figure 2 (dashed blue line) shows the transmission oscillation caused by the FP modes of a 100 μm-thick Si slab. When an x-polarized plane wave ($T_{\parallel}$, i.e. active state) excites a system of 100 μm-thick Si slab and Ge antenna, the spectra drastically change presenting a sharp transmission peak at 0.575 THz (green triangle) as seen in Figure 2 (red line). The

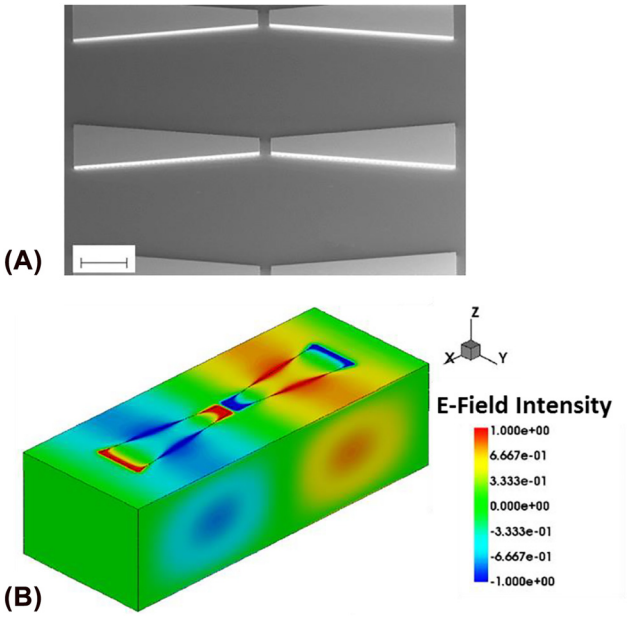

Figure 1: (A) SEM image of the fabricated n-Ge bowtie microstructure grown on Si substrates. Scale bar: 20 µm (B) Model and electric (E–) field simulation results in the antenna resonance coupling to a travelling guided mode in the substrate.

plot of the electric field at this frequency in Figure 1B reveals that this is an interaction of a TM-polarized Si slab waveguide mode and the bowtie resonant mode, i.e. a Fano interference between the bright and dark mode. The simulation confirms the mechanism of bright-mode coupling to the traveling wave, as the guided mode's dominant field is the *z*-component (Figure 1B), corresponding to a transverse magnetic mode traveling in the *x*-direction. An FP oscillation would exhibit the profile of standing waves with a dominant *E*-field in the *x*- or *y*-direction. In contrast, a *y*-polarized plane wave ($T_{\perp}$, i.e. inactive state) on the 100 µm-thick Si slab and Ge antenna system only excites the FP oscillations, shown in Figure 2 (solid blue line). The slab mode is dominated by the *z*-component of the electric field, which cannot be excited directly by the EM source. The thickness of the samples influences both, the Fano interference and the FP resonance condition. However, the reason for the efficient coupling between the antennas and a guided mode is the periodic arrangement of the antennas, *P*. The coupling occurs for an effective index-matching condition calculated as,

$$n_{\text{eff}} = mc_0/Pf_0 \tag{1}$$

where n_{eff} is the effective index calculated from the coupling condition and m is an integer mode index, P the periodic distance of the bow-tie antennas, and f_0 the frequency.

When covering the antenna with a sensing material, the Fano peak in the transmission spectrum of the active state is not expected to shift since the dark mode, unlike the bright mode, is not in direct contact with the sample. On the other hand, it is expected that the bright mode, seen as transmission minima next to the Fano peak, will be sensitive to changes in the refractive index, *n*, of its surroundings. Therefore, the transmission minimum preceding the Fano resonance is chosen as the "sensing spot" (Figure 2, black triangle).

In this study, two bow-tie antenna geometries are investigated namely "P3" with a designed $f_0 < 1$ THz (82 µm arm length) and "P4" with $f_0 > 1$ THz (46 µm arm length). Standard, 200-mm Si substrates or Silicon-On-Insulator (SOI) substrates (Si/2 µm SiO_2)/200 nm Si) are used for the epitaxial growth of Ge, with a target Ge thickness of ~1.5 µm. After the fabrication of the highly n-doped (10^{19} cm^{-3}) Ge antennas a protective Si_3N_4 layer (30–60 nm) can be deposited. To reduce the standard Si substrate thickness (~730 µm), an automatic chemical-mechanical polishing process was performed on the back-side of the 200-mm wafer. Further details can be found in section VII and in [14].

2.2 Theoretical and experimental results

A THz TDS with a polarized source was used in transmission mode (see section VII). The experimental (Figure 3A) and simulated (Figure 3B) spectra for the P3 antenna design on 65 µm-thick Si substrates are evaluated

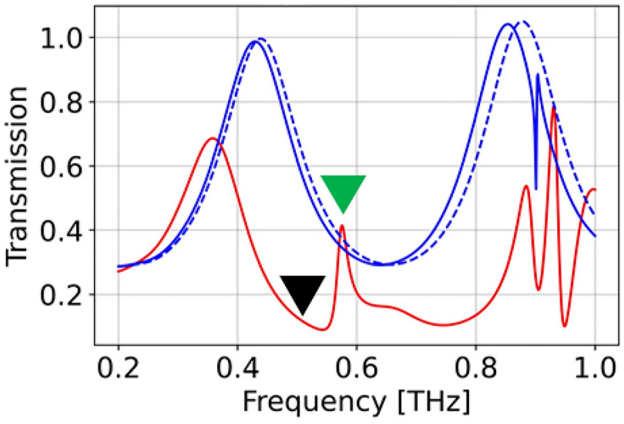

Figure 2: Transmission spectra for vertical plane wave illuminating a Si slab of 100 um thickness (dashed blue line), *y*-polarized illumination of the system Si slab and Ge bowtie antennas (solid blue line) and *x*-polarized illumination of the same (red line).

as the transmission ratio between the spectra excited parallel to the antenna arm ($T_{\parallel}$) and the spectra with polarization perpendicular to the antenna arm ($T_{\perp}$), i.e. active-to-inactive dichroic ratio. In Figures 3A, B, it can be seen that in the range 0.4 THz < f < 0.9 THz the spectra of active antenna/thinned substrate structure and antenna/thick substrate present a large difference in their transmission characteristics. This clearly indicates the activation of the THz resonance in the n-Ge/Si-slab system. The Fano transmission peak can be seen in the spectrum at around 0.7 THz, confirming the presence of a dark mode and its successful interaction with the bright mode. This can be compared to the spectra of the stand-alone bright mode, i.e. without Fano interference, on a 730 µm thick substrate (Figure 3A, black dashed line). The stand-alone bright mode (antenna resonance) of the 730 µm-thick substrate presents several local maxima and minima in transmission, caused by the FP oscillations due to its larger thickness, with an overall trend to reach a global minimum. A Lorentzian fit centers this antenna resonance at f_c~0.8 THz, with an approximate Q-factor of 1.9 ($Q = f_c$/FWHM). Comparing these results it is clear that the use of 65 µm-thick substrates has the intrinsic benefit of drastically reducing the FP oscillations. More importantly, due to the Fano coupling the width of the antenna resonance, i.e. the sensing-peak, is effectively reduced, increasing the Q-factor to ~3.

To evaluate the influence of the Si slab thickness (t) on the resonance characteristics on P3 antenna geometry a Figure of Merit (FOM) is introduced, as

$$\text{FOM} = S/\text{FWHM} \tag{2}$$

where sensitivity, $S = \Delta f_c/\Delta n$, is defined as the frequency shift of the experimental resonance center frequency (Δf_c) for a change in refractive index (Δn), and FWHM the full width at half maximum of the resonance. As seen in Figure 3B, the FOM and Q-factor increases directly with the substrate thickness in the 60 µm < t < 80 µm range.

The strength of the Fano coupling is predicted to depend on the angle between the antenna arm and the polarization of the incident radiation. In Figure 4A, we plot both experimental and theoretical THz transmission spectra at different incident angles ($T_\circ$), normalized to the inactive state $T_{\perp}$ (90°). The experimental results agree with the simulations of angular dependency.

The experimental data of the sensing-peak (Figure 4A, shaded area) can then be fitted to evaluate the angular dependence of f_c and Q-factor, as shown in Figure 4B. As the angle between the polarized THz radiation and the antenna's arm is reduced to 0°, i.e. $T_{\parallel}$, the fitted value of f_c increases. A direct relation is also observed for the Q-factor which clearly indicates a reduction of its FWHM.

To study the coupling conditions of the n-Ge antenna/Si slab system for different substrate thicknesses, complete

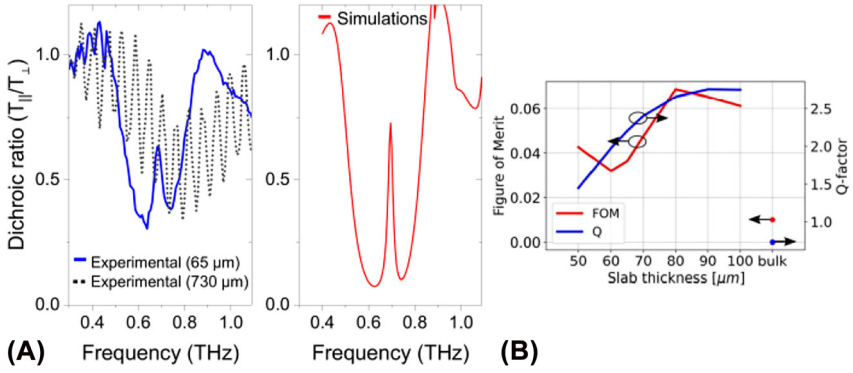

Figure 3: (A) Experimental (blue line) and simulated (red line) dichroic transmission ratio of the antenna resonance coupled to a 65 µm-thick substrate. The antenna resonance on a 730 µm-thick substrate (black dashed line) is shown for comparison (B) Simulation results of FOM and Q-factor of the coupled (fano) resonance versus substrate slab thickness.

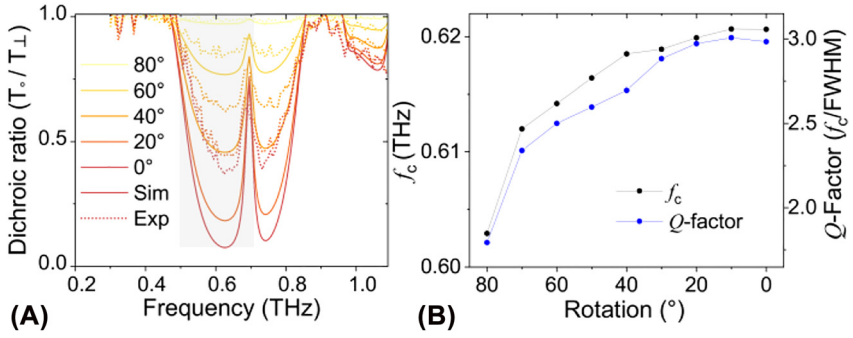

Figure 4: (A) Angular dependency of the fano coupling to the incident THz wave. (B) Angular dependency of the Q-factor and f_c of a Lorentz fit to the sensing-peak.

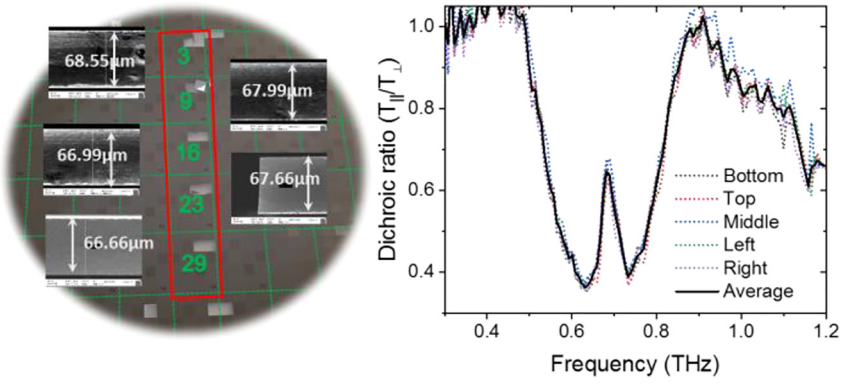

Figure 5: Thickness and THz spectra sampling from the wafer-scale grinding process for a target thickness of 65 µm.

200 mm wafers were automatically thinned-down at IHP's CMOS pilot line. As example, Figure 5 shows an optical image of the wafer and the sampling of the substrate thickness. A sampling of the thinnest target thickness (65 µm) was performed by SEM cross-section to assess the precision of the automatic grinding process. A maximum substrate thickness difference of 3 µm was observed between samples on the same wafer. Additionally, variations of the THz spectra between random samples on the wafer (Figure 5) and from the repetitive measurement of the same sample was found to have a variation <3 GHz in f_c of the sensing-peak.

Using Eq. (1) and the dispersion relation for the slab modes, a coupling diagram is calculated and presented in Figure 6A for a t = 65 µm Si slab and n_{slab} = 3.415 suspended in air (n_{air} = 1). The intersection of the coupling conditions (green dashed line) in Figure 6A with the TE (blue line) and TM (red line) modes of the guided traveling wave predicts the frequency at which the Fano coupling occurs. For a TM1 mode and t = 65 µm the frequency is at ~0.7 THz, as calculated and experimentally confirmed (see Figure 3). The periodic placement of the antennas P enables the Fano coupling as it enforces a periodic electric field scattered by the antennas, producing an effect akin to a resonant waveguide coupler [21]. This condition establishes the importance of matching the geometry and arrangement of the antennas to the thickness of the substrate to obtain the best coupling efficiency. Keeping the antenna-to-antenna distance fixed while increasing the slab thickness will lead to guided modes being coupled into the slab at lower frequencies due to the change in the dispersion relation. Following the theoretical calculations, the effect of a 75 and 85 µm-thick wafer on the Fano coupling were studied. In Figures 6B, C, the $T_{\parallel}$ transmission of 75 and 85 µm-thick, is shown respectively, referenced to that of air, T_{air}. As predicted by theory, the Fano peak shows a red shift as the substrate thickness increases. Fitting of the sensing-peak, renders a Q-factor of 2.95, 3.68 and 2.89 for substrate thickness of 65, 75 and 85 µm respectively. From antenna radiation theory it is expected that the Q-factor can be further improved by the use of a high-resistivity substrate, e.g. SOI. This was studied by FEM simulations. The field enhancement at the antenna gap can be compared in Figure 6D for P3 antennas on a Si substrate and an SOI substrate (both 75 µm thick). These results motivate the experimental exploration of the effects SOI substrates on the spectral features.

3 Biofunctionalization of Ge antennas

Tailored surface functionalization of biosensing platforms allows for targeted and sensitive detection of specific

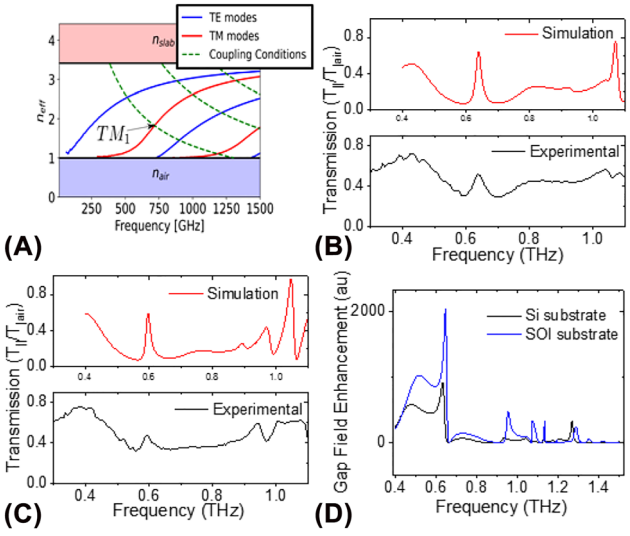

Figure 6: (A) Coupling conditions for the TE and TM modes of the traveling guided mode and n-Ge antenna resonance. Simulation and experimental normalized transmission of the antenna resonance coupled to a (B) 75 µm and (C) 85 µm-thick substrate (D) a simulation comparison of the (antenna) gap field enhancement of P3 design on a 75 µm-thick Si substrate against a 75 µm-thick SOI substrates.

biomolecules while suppressing background detection of off-target molecules, especially in complex and crowded samples. In the following, we present versatile strategies for biofunctionalization of the n-Ge antennas sensing platform for selectively capturing proteins and cells.

3.1 Site-specific protein capturing to Si_3N_4-passivated Ge resonators

As a biocompatible coating suitable for site-specific protein immobilization on the chemically inert Si_3N_4 passivation layer, Si_3N_4-coated Ge resonator wafers were surface-functionalized by using poly-L-lysine graft poly ethylene glycol) conjugated with the HaloTag ligand (PLL-PEG-HTL) [22]. After 10 min of plasma treatment, PLL-PEG-HTL in aqueous solution is rapidly adsorbed electrostatically to the negatively charged Si_3N_4 layer. This way, surface functionalization of Ge resonators becomes much faster and easier to handle compared to functionalization with α-lipoic acid established in previous work [10, 11]. The obtained PLL-PEG-HTL-functionalized Ge wafers can be employed for site-specific, covalent capturing of HaloTag-fusion proteins. Given that both Ge antennas and the Si substrate are coated with Si_3N_4, surface functionalization and protein immobilization can take place homogeneously on the whole wafer sample.

For proof-of-concept experiments, we explored the immobilization of HaloTag-mEGFP to Ge resonators. The cartoon in Figure 7A depicts the self-assembly of PLL-PEG-HTL on Si_3N_4 coated Ge and Si surfaces and subsequent capturing of HaloTag-mEGFP to the HaloTag ligand (HTL). The obtained samples were analyzed with fluorescence confocal laser scanning microscopy (CLSM). To reduce background signals due to laser reflection of the substrate surface, we used the 458 nm laser line of a multiline argon laser to excite the mEGFP chromophore. Fluorescence emission was collected with a 500–550 nm bandpass filter. Photobleaching of a defined ROI enabled us to quantify fluorescence intensities of specifically immobilized HaloTag-mEGFP at Ge antennas and the Si substrate. The differences of total fluorescence intensity and the intensity measured in the bleached region are shown in Figure 7B, C. As a negative control, Ge resonator wafers coated with non-functional PLL-PEG (PLL-PEG-OMe) were incubated with HaloTag-mEGFP.

Comparison of fluorescence intensities obtained for samples functionalized with PLL-PEG-HTL, PLL-PEG-OMe and non-functionalized Ge resonators clearly established highly specific protein immobilization to PLL-PEG-HTL (Figure 7D).

No unspecific protein binding was observed for PLL-PEG-OMe functionalized samples (Figure 7D). Thus, PLL-PEG shields the wafer surface from unspecific binding very efficiently and the HTL moieties enable efficient immobilization of HaloTag-fusion proteins to the Si_3N_4-coated Ge resonator. The PLL-PEG-based surface functionalization enables tailoring of the capturing specificity by exchanging the functional unit (here HTL) to alternative affinity moieties. For instance, the applications can be extended for the formation of focal adhesions of cells by using RGD (see below), immobilization of anti-ALFA-tag nanobodies using the ALFA-tag [23], or immobilization of oligohistidine-tagged proteins using trisNTA [24].

3.2 Interfacing cells with Ge resonators

Inspired by the successful *in vitro* capturing of proteins on Ge resonators, we turned to facilitate the direct transfer of

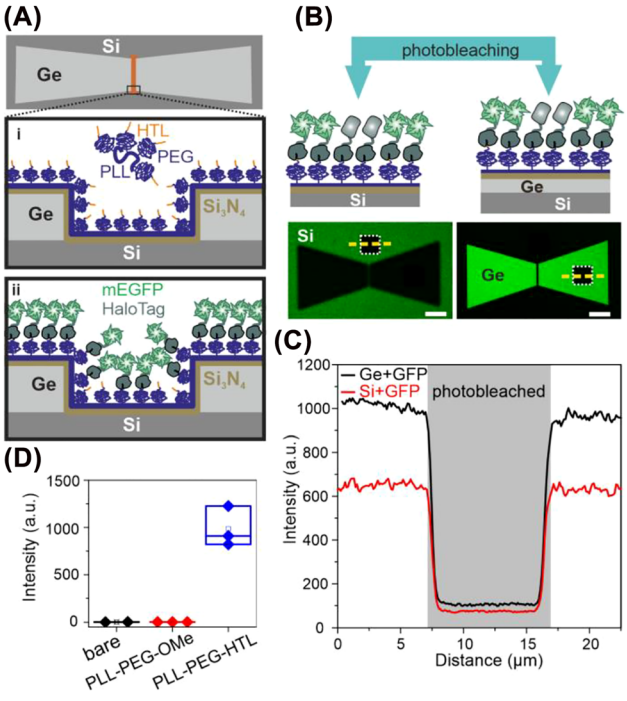

Figure 7: Specific protein capturing to PLL-PEG-HTL-functionalized Ge resonators. (A) Cartoon depicting surface functionalization of Si_3N_4-coated Ge antennas by PLL-PEG-HTL (i) and subsequent immobilization of HaloTag-mEGFP (ii). (B) After protein immobilization, a selected area on a Ge antenna (right) and on the Si substrate (left) were photobleached by the confocal laser beam (white dotted squares) to determine the background signal. Scale bars: 10 μm (C) Fluorescence intensity profiles along the yellow dotted line depicted (B) were analyzed to quantify protein binding (D) background-corrected fluorescence intensities after incubating PLL-PEG-HTL and PLL-PEG-OMe functionalized Ge-antennas as compared to bare Si_3N_4-coated Ge resonators.

proteins from cells into the THz hotspots at the gap of Ge antennas. The efficient transfer of proteins from cells requires precise control of cell attachment and three-dimensional interfacing with the substrate. For steering cell adhesion on Ge resonators, we functionalized unpassivated Ge antennas with a peptide Ac-CGRGDS-COOH. The cysteine residue of the peptide can selectively bind to Ge while the RGD motif acts as the tethering side of integrins in cells to form focal adhesions (see Figure 8A). To avoid cell attachment to the Si substrate, the substrate was backfilled with PLL-PEG-OMe. On such obtained Ge resonator wafers, HeLa cells stably expressing lifeact-mEGFP were cultured for 6 h. SEM (Figure 8B) and fluorescence CLSM (Figure 8C) imaging confirmed the selective growth of cells on the Ge antennas. Strikingly, the cell morphology adapted to the Ge antenna geometry (Figure 8B–D) which clearly supports selective RGD peptide modification on the Ge antennas.

This proof-of-concept thus demonstrates selective interfacing of cells with unpassivated Ge resonators. To achieve selective interfacing of cells with passivated Ge resonators, the Ge antenna surface can be selectively functionalized with PLL-PEG-RGD via microcontact printing, as previously shown for silicon micropillar arrays [25]. Based on the results, specific capturing of target proteins directly from cells into the THz hotspot can be envisaged by engineering a selective biofunctionalization at the gap of the Ge antennas.

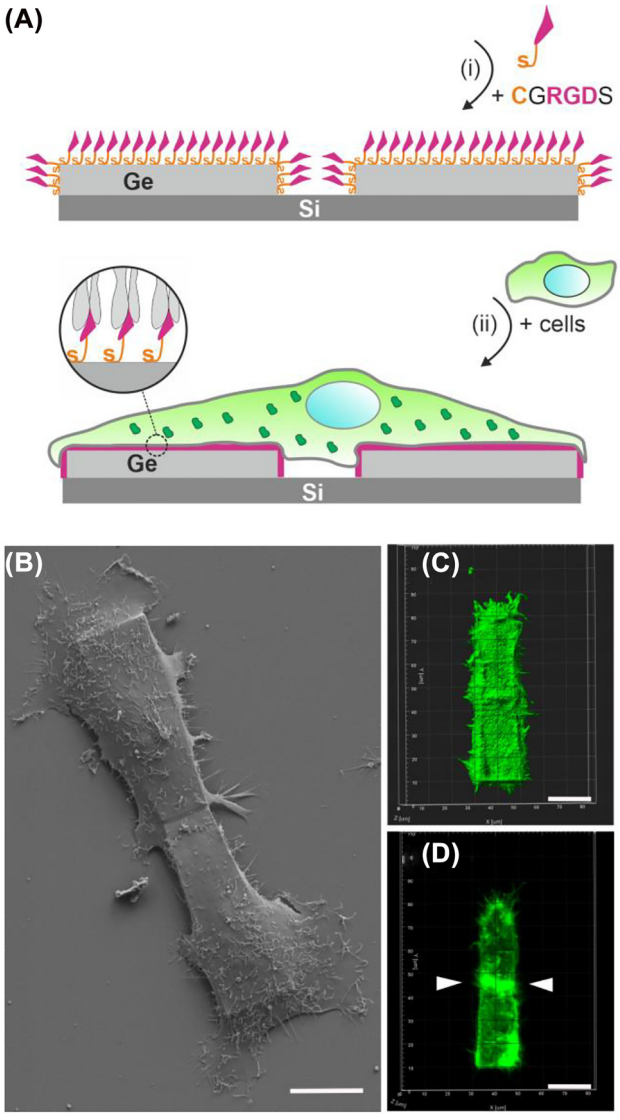

Figure 8: Interfacing Ge-resonators with human cells. (A) Cartoon depicting self-assembly of Ac-**CGRGDS**-COOH on the surface of an unpassivated Ge resonator (i) to promote selective cell attachment (ii). (B) Representative SEM image of a HeLa cell growing on a Ge resonator. (C), (D) fluorescence CLSM images of a HeLa cell expressing lifeact-mEGFP while morphologically adapting to the Ge resonator geometry. (C) 3D reconstruction of an image z-stack of a HeLa cell on a Ge resonator. (D) image slice of the z-stack shown in (C) with arrows indicating the resonator gap region. Scale bars 20 µm.

4 Biosensing results

Serum albumins make up the most abundant fraction of water-soluble proteins in the blood plasma [26]. Bovine Serum Albumin (BSA) has become a common model protein for biosensing applications [27–29] as it is readily available commercially, stable and its optical properties are well known [30, 31]. Here, simple BSA-multilayers are employed in proof-of-principle experiments to outline the sensing performance of the n-Ge antenna platform.

The Fano coupling of P3 ($f_0 < 1$ THz) and P4 ($f_0 > 1$ THz) antenna designs on Si and SOI substrates was studied. As a proof-of-principle for sensing, the same set of samples is used to detect the presence of BSA with a concentration of 150 µmol/L (BSA10, 150 µM) on the surface of the n-Ge antennas/Si substrate system. As reference, the normal concentration range of serum albumin in human plasma is 35–50 mg/ml (i.e. 526–750 µM) [32]. Based on SEM cross-section images, the incubation of BSA150 is expected to leave a layer with a thickness of a few hundred nanometers. Materials in the vicinity of the plasmonic antennas produce a change in the dielectric environment which affects the f_0 resonance conditions. This is expected to be seen experimentally as a shift in the center frequency (Δf_c) of the sensing-peak.

Spectral shifts usually imply a variation in the transmission through the antennas. Variation in the transmitted power is a commonly used detection concept in sensors, such as those found in e.g. CO_2 monitors. Thus, using as a

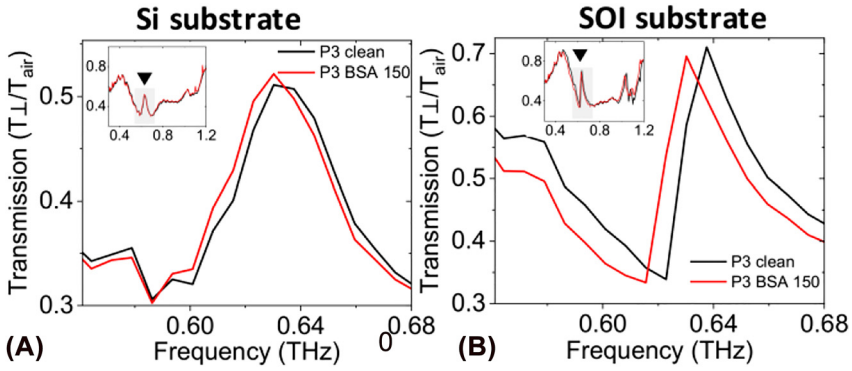

Figure 9: Normalized transmission spectra at the fano resonance of clean (black lines) and with an albumin layer (red lines) P3 antennas (f_0 <1 THz) grown on 75 μm-thick (A) Si and (B) SOI substrates. Note the increase of the fano resonance sharpness in SOI substrates (shaded area) due to the gap field enhancement. Insets: Extended frequency range of spectra. Resonance indicated by the black triangles and shadow area.

reference the transmission with a clear path (air) resembles a more practical scenario than the transmission of antennas in the inactive state. The transmission of uncoated P3 antennas (black lines) in the active state (Fano resonance) referenced to air ($T_{\parallel}/T_{\text{air}}$) on 75 μm-thick Si and SOI substrates is shown in Figure 9A, B, respectively. It can be observed that as predicted by simulations the spectral features on SOI substrates maintain their general shape (compare insets of Figure 9A, B) but are enhanced in intensity, mostly in the vicinity of the Fano coupling. Due to the SOI substrate, the sensing-peak (black triangles in insets) exhibits a width reduction of over 30%, and a highly sharp change from 71 to 33% in transmission. The effect on the resonance due to the incubation of BSA150 layers (red lines) can be seen as well in Figure 9A, B. A red shift of the spectra, due to the change in the refractive index, is observed for both substrates.

Similarly, the response of P4 antenna designs on 75 μm-thick Si (Figure 10A) and SOI substrates (Figure 10B) was compared. As anticipated from Eq. (1) and Figure 6A, the Fano coupling appears as well although the thickness was not engineered for P4 antenna geometry. This results in a sensing-peak (black triangle) wider than P3 designs. The use of SOI substrate for P4 antennas enhances as well the sharpness of the spectral features producing a change in transmission from 70 to 28% within 65 GHz. The presence of BSA150 layers (blue lines in Figure 10) on P4 antennas response has a broader spectral shift in the sensing-peak over a wider range.

5 Discussion

The geometric characteristics of P3 and P4 designs produce two different f_c which in turn produces different conditions for the Fano coupling. At the low end of the spectrum, both designs present a transmission peak centered just above 0.4 THz. While this feature is intrinsic to the substrate thickness, i.e. FP oscillations (see section II), it is still influenced by both the presence of n-Ge antennas and the properties of the substrate. It can be seen how the FP oscillations are disturbed by the onset of Fano coupling in P3 design, while in P4 the same oscillation is largely unaffected. Close to their designed f_0, both designs present the characteristic asymmetric shape of Fano resonance, i.e. a transmission peak preceded by a global transmission minimum. As expected, the use of a high-resistivity substrate increased the intensity of these spectral features. This can be understood from the low-loss substrate for the resonators, whose effect is independent of the Fano coupling, i.e. the resonance on 730 μm-thick SOI will have a larger Q-factor than on 730 μm-thick Si substrate.

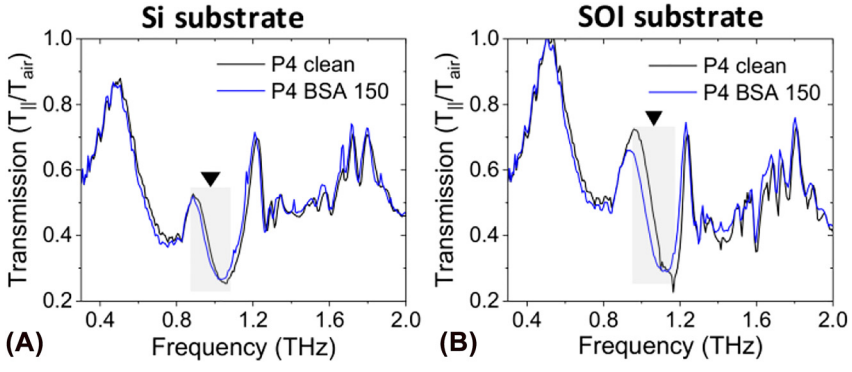

Figure 10: Normalized transmission spectra of clean (black lines) and with an albumin layer (blue lines) P4 antennas (f_0 > 1 THz) grown on 75 μm-thick (A) Si and (B) SOI substrates. Fano resonances indicated with black triangles and a shadowed area.

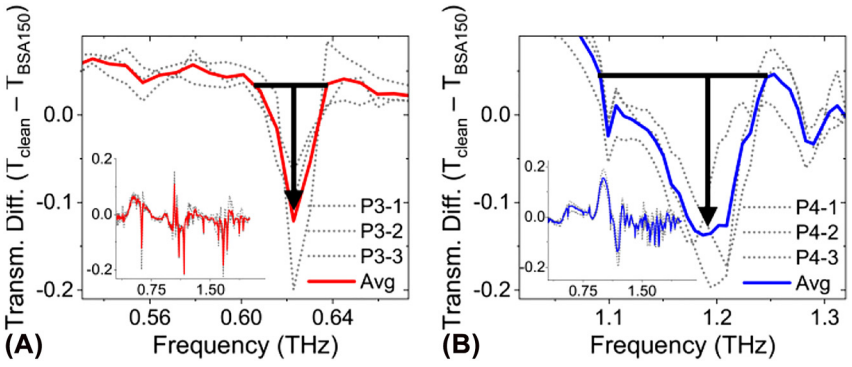

Figure 11: Comparison of the transmission contrast (T_{clean}–T_{BSA150}) between fano resonances coupled to (A) P3 and (B) P4 designs. Insets: Transmission differential for the whole range, respectively.

However, the strong sharpening effect of the SOI in P3 samples can be understood as an improvement of the Fano coupling efficiency due to lower refractive index contrast. At an interface, a lower refractive index contrast reduces reflections of the surface. In the case of P3 antennas on 65 µm-thick substrates, the coupling of the TM1 dark mode occurs close to a $n_{eff} \sim 2$ (see Figure 6A). Similarly, the refractive index of the buried SiO_2 layer ($n \sim 1.98$) is a closer match to the n_{eff} of the Fano coupling conditions for P3 on 75 µm-thick substrates. On the other hand, the wider resonance of P4 could be explained by a larger n contrast since the intersection to the coupling conditions takes place at larger n_{eff} due to the antenna design.

The presence of BSA150, as expected produces a Δn and consequently a red shift of the resonance. Considering a non-dispersive refractive index of BSA150 within the spectrum of interest, P4 delivers a better performance in terms of sensitivity S as defined in Section II, i.e. it shows a larger Δf_c for the same Δn. This can be understood by the periodicity P and geometry of P4 designs which doubles the number of antennas per mm^2. From a different perspective, the transmission contrast (T_{clean}–T_{BSA10}) could be used to compare the response of P3 and P4 designs, as shown in Figure 11A, B, respectively. Following the average transmission contrast of three different experiments using P3 antennas, it can be seen that an average transmission change of >10% occurs sharply at ~0.62 THz P4 antennas present an average transmission change of similar magnitude at ~1.19 THz. However, the transmission change in P4 occurs within a bandwidth of ~100 GHz while for P3 is only ~20 GHz. This explorative comparison of different geometries offers a glimpse of further improvements that can be engineered to increase Δf_c and with it S e.g. increasing the antenna density, while still maintain sharp spectral features. It can be noted that the sudden transmission variation in P3 antennas takes place in a bandwidth only one order of magnitude larger than the maximum resolution of the THz TDS system (1.2 GHz). This highlights how the advances in antenna engineering are closing the limits of our current measuring capabilities. As an outlook, the practical application of n-Ge plasmonic antennas as a sensor platform can be envisioned as e.g. a compact sensing equipment assembled together with an all-electronic THz TRx system. Sensing events happening within narrow bandwidths are an added benefit that relaxes the circuit complexity, reducing at the same time possible error sources coming from n-dispersive analytes.

6 Conclusions

Highly n-doped Ge plasmonic antennas on 200-mm Si and SOI wafers were produced and automatically thinned down in a CMOS fabrication pilot line at IHP. As predicted by theoretical simulations, a Fano-like resonance arises from the coupling of the Ge antenna resonance (bright mode) with a traveling wave (dark mode) guided in thinned-down Si slabs. As a consequence, the spectral characteristics of the THz resonance, such as the Q-factor, have been improved beyond the intrinsic material properties with the added benefit of removing transmission variations due to FP oscillations. A second improvement stage presented in this work was the use of high-resistance SOI substrates. Sophisticated biofunctionalization strategies were developed in parallel to basic biosensing experiments, demonstrating versatile, fast and easy-to-handle surface-functionalization of Ge-resonators. Biofunctionlization of the plasmonic antennas for site-specific capturing of protein monolayers has been established, using a copolymer with a poly (L-lysine) base and poly(ethylene glycol) chains fused to the HaloTag-Ligand (PLL-PEG-HTL) as a functional moiety. An exchange of the functional moiety allows for future tailoring of the specificity of the PLL-PEG towards a broad variety of molecular-tags, proteins and cells. Additionally, the Ge-selective interfacing of unpassivated Ge resonators with cells using the peptide Ac-CGRDS-COOH has been

shown. This represents a first step towards *in-situ* protein capturing from cells growing on the sensor surface. As proof-of-principle for protein sensing, BSA multilayers were deposited on the surface of the antenna samples. The sensitivity and transmission characteristics of two antenna geometries along with its Fano coupling efficiency were compared. The results show that the BSA layer produced a change of over 10% in transmission, with a very narrow bandwidth of only 20 GHz.

The use of semiconductor-based plasmonics allows the integration of an innovative THz biosensing platform in the conventional CMOS fabrication environment. Due to the advances in technology and circuit designs, reaching hundreds of GHz in operation, the n-Ge plasmonic antenna technology has the potential to coalesce with the available SiGe mixed-signal ecosystem. High-frequency TRx systems assembled with the plasmonic sensing platform could enable the use of compact, economic and portable detectors in the future.

7 Materials and methods

7.1 N-Ge antennas fabrication and THz characterization

The deposition of n-doped Ge layers on slightly p-doped Si substrates Si (001) wafers (200 mm) has been carried out using an ASM Epsilon 2000 lamp-heated reduced-pressure chemical vapor deposition (RPCVD) single wafer system. The experimental spectral response of the antennas has been obtained in atmospheric conditions by Terahertz Time-Domain Spectroscopy (THz-TDS), with a spectral bandwidth of 5 THz, 90 dB dynamic range and a frequency resolution of ~5 GHz (Terasmart from Menlo Systems, Germany). The THz-TDS was in transmission-mode setup with a linearly polarized source, placing the samples at the THz focus (approximately 3 mm in diameter). The spurious THz lines of atmospheric humidity are largely removed by the reference measurements. Spectra were collected by aligning the long axis of the antenna arms parallel to the electric field polarization ($T_{\updownarrow}$), thus activating the antenna resonance, and, as a reference, either the long antenna axis perpendicular to the electric field polarization ($T_{\perp}$) or a clear path (T_{air}). To study the effect of substrate thickness on the spectral response of the antennas, wafer-scale polishing of the backside of the substrates was automatically performed using an Accretech AD3000T-HC system. Due to the fragility of thinned-down dies, a Dicing Before Grinding (DFG) process was performed by a Disco DFG8540 system. As expected, Fabry-Perot (FP) oscillations related to the substrate thickness varied accordingly, with the oscillations period increasing as the substrate is thinned down.

7.2 Ge resonator functionalization and protein immobilization

HaloTag ligand-functionalized poly-L-lysine-*graft*-(polyethylene glycol) copolymer (PLL-PEG-HTL) was prepared as described previously in [33]. PLL-PEG-methoxy (PLL-PEG-OMe) preparation follows a one-step reaction protocol. 20 mg OMe-PEG-COOH (Mw: 2000 Da, Rapp Polymere GmbH), 7.5 mg poly-L-lysine hydrobromide (Mw: 15.000–30.000 Da, Merck) and 8 mg of EDC (Mw: 192, Carl Roth GmbH + Co. KG) were dissolved in 400 µl 2-(4-(2-hydroxyethyl)-1-piperazineethanesulfonic acid (HEPES) buffer (100 mM HEPES, pH 7.5). After stirring for 7–8 h at room temperature, the mixture solution was dialyzed against MilliQ water for 24 h. The sample was lyophilized, resulting in a white powder and stored at −20 °C. Functionalization of plasma cleaned (low-pressure plasma system Femto, diener electronics) Ge resonator wafers was achieved by dip-coating the Ge resonator wafer in 1 mg/ml PLL-PEG-HTL (1 mg/ml) for 10 min. Subsequently, the wafer was rinsed in fresh ultrapure water and dried under a nitrogen stream. HaloTag-mEGFP fusion protein was produced as previously described in [22, 34]. For immobilization of HaloTag-mEGFP, Ge resonator wafers functionalized with PLL-PEG-HTL were incubated in 3 µM HaloTag-mEGFP dissolved in HBS buffer (20 mM HEPES/NaOH, pH 7.5, 150 mM NaCl) for 1 h. To confirm specific protein capturing, the same experimental conditions were used for incubating HaloTag-mEGFP on a Ge resonator wafer coated with PLL-PEG-OMe as negative controls.

7.3 Cell culture on Ge resonators

To allow selective cell growth on bare Ge resonators, samples were sonicated in 2-Propanol (Sigma-Aldrich, 190,764) to remove coarse organic residue for 5 min. Subsequently, samples were incubated with 2 M citric acid (Carl Roth GmbH + Co. KG) at room temperature for 5 min to remove the native oxides on the Ge surface [35]. Samples were incubated 1.5 h with 1 mM Ac-CGRGDS-COOH peptide (custom-synthesized byCoring System GmbH, Gernsheim/Germany) dissolved in HBS buffer (20 mM HEPES, 150 mM NaCl, pH 7.5) to provide binding sites for focal adhesion via the RGD motif. The cysteine of the peptide allows selective functionalization of the germanium resonators on the silicon oxide wafer. After incubation, samples were washed in ultrapure water and dried with nitrogen. The remaining silicon oxide surface was subsequently passivated by incubation with PLL-PEG-OMe (1 mg/ml) for 20 min. Samples were washed in ultrapure water and dried with nitrogen. HeLa cells stably expressing lifeact-mEGFP ('HeLa lifeact-mEGFP') [36] were cultivated at 37 °C and 5% CO_2 in MEM's Earle's with stable glutamine (Biochrom AG, FG0325) supplemented with 10% fetal bovine serum (FBS) (Biochrom AG, S0615), 1% non-essential amino acids (PAA laboratories GmbH M11003) and 1% HEPES buffer as well as 0.8 µg/ml G418 (Calbiochem 345,810). 20 h after seeding on Ac-CGRGDS-COOH functionalized Ge resonators, stable cell attachment was obtained for fluorescence CLSM imaging.

7.4 Confocal fluorescence laser scanning microscopy

Fluorescence images were acquired with an upright microscope (Axio Imager.Z1, Zeiss), equipped with a confocal laser scanning system (LSM 510 Meta NLO, Zeiss) and a ×|63|× water dipping objective (W Plan Apochromat/NA 1.0 Vis-IR, Zeiss) at a sampling resolution of 58.93 nm/pixel. The 458 nm line of a multi-line Argon laser was used for excitation of mEGFP. Emission was detected with a bandpass filter of 500–550 nm. For the microscopy imaging, chips were deposited in microscopy sample chambers with the Ge resonators faced towards the objective. For the photobleaching assays, a rectangle area of

10×10 µm was bleached by 405/458/488 nm excitation for 60 s with a laser power of 7.5 mW measured at the objectives, followed by acquisition using 0.5 mW 458 nm laser excitation.

7.5 Scanning electron microscopy of cells on Ge resonators

For scanning electron microscopy (SEM) of cells cultured on Ge resonators, samples were fixed 20 h after seeding. After treatment for 1 h with 2.5% glutaraldehyde in 0.1 M phosphate buffered saline (PBS), pH 7.4 at room temperature, samples were stepwise dehydrated in a graded ethanol series. Samples were critical-point dried in 100% ethanol with a critical-point-dryer (Balzers, Switzerland). Dried samples were mounted onto aluminum stubs with conducting leit-tabs (Plano GmbH) and coated with platinum-iridium to a thickness of 10 nm. SEM images were acquired with a Zeiss Auriga scanning electron microscope operated with an in-lens detector at 4 kV.

Acknowledgment: The work presented has been funded in part by the German Research Foundation (DFG) within the project ESSENCE (Electromagnetic Sensors for the Life Sciences).

Author contributions: All the authors have accepted responsibility for the entire content of this submitted manuscript and approved submission.

Research funding: Funder Name: Deutsche Forschungsgemeinschaft, Funder Id: 10.13039/501100001659, Grant Number: ESSENCE Program 272553338.

Conflict of interest statement: The authors declare no conflicts of interest regarding this article.

References

[1] Y.-S. Lee, *Principles of Terahertz Science and Technology*, New York, Springer Science+Business Media, LLC, 2009.

[2] N. Rothbart, O. Holz, R. Koczulla, K. Schmalz, and H.-W. Hübers, "Analysis of human breath by millimeter-wave/terahertz spectroscopy," *Sensors*, vol. 19, no. 12, p. 2719, 2019.

[3] M. Danciu, T. Alexa-Stratulat, C. Stefanescu, et al., "Terahertz spectroscopy and imaging: a cutting-edge method for diagnosing digestive cancers," *Materials*, vol. 12, no. 1519, 2019, https://doi.org/10.3390/ma12091519.

[4] M. Naftaly, N. Vieweg, and A. Deninger, "Industrial applications of terahertz sensing: state of play," *Sensors*, vol. 19, no. 4203, 2019, https://doi.org/10.3390/s19194203.

[5] A. Markelz, S. Whitmire, J. Hillebrecht, and R. Birge, "THz time domain spectroscopy of biomolecular conformational modes," *Phys. Med. Biol.*, vol. 47, no. 21, pp. 3797–3805, 2002.

[6] K. Schmalz, N. Rothbart, M. H. Eissa, J. Borngräber, D. Kissinger, and H.-W. Hübers, "Transmitters and receivers in SiGe BiCMOS technology for sensitive gas spectroscopy at 222 - 270 GHz," *AIP Adv.*, vol. 9, no. 1, 2019, Art no. 015213.

[7] Z. Hu, M. Kaynak, and R. Han, "High-power radiation at 1 THz in silicon: a fully scalable array using a multi-functional radiating mesh structure," *IEEE J. Solid State Circ.*, vol. 53, no. 5, pp. 1313–1327, 2018.

[8] P. Hillger, M. van Delden, U. S. M. Thanthrige, et al., "Toward mobile integrated electronic systems at THz frequencies," *J. Infrared, Millim. Terahertz Waves*, vol. 41, pp. 846–869, 2020.

[9] S. Enoch, *Plasmonics: From Basics to Advanced Topics*, Berlin, Heidelberg, Springer, 2012.

[10] M. Bettenhausen, F. Römer, B. Witzigmann, et al., "Germanium plasmon enhanced resonators for label-free terahertz protein sensing," *Frequenz*, vol. 72, nos. 3–4, pp. 113–122, 2018.

[11] M. Kazmierczak, J. Flesch, J. Mitzloff, et al., "Stable and selective self-assembly of α-lipoic acid on Ge(001) for biomolecule immobilization," *J. Appl. Phys.*, vol. 123, no. 17, 2018, Art no. 175305.

[12] E. Mauriz, "Recent progress in plasmonic biosensing schemes for virus detection," *Sensors*, vol. 20, no. 17, 2020, https://doi.org/10.3390/s20174745.

[13] S. Gruessing, B. Witzigmann, F. Roemer, et al., *Modeling of Plasmonic Semiconductor THz antennas in Square and Hexagonal Array Arrangements*, San FranciscoUnited States, SPIE OPTO, California, 2020.

[14] C. A. Chavarin, E. Hardt, S. Gruessing, et al., "n-type Ge/Si antennas for THz sensing," *Opt Express*, vol. 29, no. 5, pp. 7680–7689, 2021.

[15] M. F. Limonov, "Fano resonance for applications," *Adv. Opt. Photon*, vol. 13, no. 3, pp. 703–771, 2021.

[16] U. Fano, "Effects of configuration interaction on intensities and phase shifts," *Phys. Rev.*, vol. 124, no. 6, pp. 1866–1878, 1961.

[17] R. Xu, Z. Zhang, A. D. Wieck, and N. Jukam, "Terahertz Fano resonances induced by combining metamaterial modes of the same symmetry," *Opt. Express*, vol. 28, no. 3, pp. 3932–3941, 2020.

[18] Q. Xie, G. Dong, B. Wang, and W. Huang, "High-Q fano resonance in terahertz frequency based on an asymmetric metamaterial resonator," *Nanoscale Res. Lett.*, vol. 13, no. 294, 2018, https://doi.org/10.1186/s11671-018-2677-0.

[19] R. Singh, I. A. I. Al-Naib, M. Koch, and W. Zhang, "Sharp Fano resonances in THz metamaterials," *Opt Express*, vol. 19, no. 7, pp. 6312–6319, 2011.

[20] B. Peng, S. K. Özdemir, W. Chen, F. Nori, and L. Yang, "What is and what is not electromagnetically induced transparency in whispering-gallery microcavities," *Nat. Commun.*, p. 5082, 2014, https://doi.org/10.1038/ncomms6082.

[21] F. Gambino, M. Giaquinto, A. Ricciardi, and A. Cusano, "A review on dielectric resonant gratings: mitigation of finite size and Gaussian beam size effects," *Results Opt.*, vol. 6, no. 100210, 2022, https://doi.org/10.1016/j.rio.2021.100210.

[22] T. Wedeking, S. Löchte, O. Birkholz, et al., "Spatiotemporally controlled reorganization of signaling complexes in the plasma membrane of living cells," *Small*, vol. 11, pp. 5912–5918, 2015.

[23] H. Gotzke and M. Kilisch, M. Martínez-Carranza, et al., "The ALFA-tag is a highly versatile tool for nanobody-based bioscience applications," *Nat. Commun.*, vol. 10, no. 1, p. 4403, 2019.

[24] C. You and J. Piehler, "Multivalent chelators for spatially and temporally controlled protein functionalization," *Anal. Bioanal. Chem.*, vol. 406, no. 14, pp. 3345–3357, 2014.

[25] J. Flesch, M. Bettenhausen, M. Kazmierczak, et al., "Three-dimensional interfacing of cells with hierarchical silicon nano/microstructures for midinfrared interrogation of in situ captured

proteins," *ACS Appl. Mater. Interfaces*, pp. 8049–8059, 2021, https://doi.org/10.1021/acsami.0c22421.
[26] L. Roufegarinejad, A. Jahanban-Esfahlan, S. Sajed-Amin, and M. V. Panahi-Azar, "Molecular interactions of thymol with bovine serum albumin: spectroscopic and molecular docking studies," *J. Mol. Recogn.*, 2018, https://doi.org/10.1002/jmr.2704.
[27] S. Ge, J. Lu, M. Yan, F. Yu, J. Yu, and X. Sun, "Fluorescence resonance energy transfer sensor between quantum dot donors and neutral red acceptors and its detection of BSA in micelles," *Dyes Pigments*, pp. 304–308, 2011, https://doi.org/10.1016/j.dyepig.2011.05.013.
[28] S. Balendhran, S. Walia, M. Alsaif, et al., "Field effect biosensing platform based on 2D α-MoO3," *ACS Nano*, pp. 9753–9760, 2013, https://doi.org/10.1021/nn403241f.
[29] S. Schintke and E. Frau, "Modulated 3D cross-correlation dynamic light scattering applications for optical biosensing and time-dependent monitoring of nanoparticle-biofluid interactions," *Appl. Sci*, vol. 10, no. 24, p. 8969, 2020.
[30] H. Arwin, "Optical properties of thin layers of bovine serum albumin, γ-globulin, and hemoglobin," *Appl. Spectrosc*, vol. 40, no. 3, pp. 313–318, 1986.
[31] E. J. Cohn, W. L. Hughes, and J. H. Weare, "Preparation and properties of serum and plasma proteins. XIII. Crystallization of serum albumins from ethanol-water mixtures," *J. Am. Chem. Soc.*, pp. 1753–1761, 1947, https://doi.org/10.1021/ja01199a051.
[32] M. Corti, J. Guralnik, M. Salive, and J. Sorkin, "Serum albumin level and physical disability as predictors of mortality in older persons," *JAMA*, vol. 272, no. 13, pp. 1036–1042, 1994.
[33] T. Wedeking, S. Löchte, C. P. Richter, M. Bhagawati, J. Piehler, and C. You, "Single cell GFP-trap reveals stoichiometry and dynamics of cytosolic protein complexes," *Nano Lett.*, vol. 15, no. 5, pp. 3610–3615, 2015.
[34] S. Löchte, S. Waichman, O. Beutel, C. You, and J. Piehler, "Live cell micropatterning reveals the dynamics of signaling complexes at the plasma membrane," *JCB (J. Cell Biol.)*, vol. 207, no. 3, pp. 407–418, 2014.
[35] G. Collins, D. Aureau, J. D. Holmes, A. Etcheberry, and C. O'Dwyer, "Germanium oxide removal by citric acid and thiol passivation from citric acid-terminated Ge(100)," *Langmuir*, vol. 30, no. 47, pp. 14123–14127, 2014.
[36] S. Wilmes, M. Staufenbiel, D. Liße, et al., "Triple-color super-resolution imaging of live cells: resolving submicroscopic receptor organization in the plasma membrane," *Angew. Chem. Int. Ed.*, vol. 51, pp. 4868–4871, 2012.